JOURNAL OF COMPUTATIONAL PHYSICS **146,** 29–57 (1998)
ARTICLE NO. CP985919

Time-Domain Numerical Simulation of a Flow-Impedance Tube

Yusuf Özyörük,* Lyle N. Long,† and Michael G. Jones‡

*Department of Aeronautical Engineering, Middle East Technical University, 06531 Ankara, Turkey;
†Department of Aerospace Engineering, The Pennsylvania State University, University Park, Pennsylvania 16802; ‡Lockheed Martin Engineering and Sciences Services, c/o NASA Langley Research Center, MS 463, Hampton, Virginia 23681
E-mail: ozyoruk@rorqual.cc.metu.edu.tr

Received January 21, 1997; revised December 31, 1997

An efficient method has been developed for the application of the surface acoustic impedance condition in time-domain solutions of aeroacoustic problems, such as the broadband-frequency simulation of a flow-impedance tube. The basis for this method is the standard impedance condition stated in the frequency domain as the particle displacement continuity equation. The development of the time-domain impedance condition follows the relations among the frequency, z-, and discrete-time domains and a rational function representation of the impedance in the z-domain. The resultant impedance condition consists of finite, infinite-impulse-response type, digital filter operations in the time domain, which is very suitable to computational aeroacoustics algorithms. This paper describes the present approach and discusses the time-domain numerical simulations of the NASA Langley flow-impedance tube with a constant depth ceramic tubular liner. Both single and broadband-frequency simulations are performed. Excellent agreement is shown with experimental data at various frequencies and flow conditions. © 1998 Academic Press

Key Words: flow-impedance tube; computational aeroacoustics; impedance conditions; z-transforms; nonreflecting boundary conditions; finite difference.

1. INTRODUCTION

The development of time-domain surface acoustic impedance conditions is necessary for realistic applications of computational aeroacoustics (CAA) techniques, such as the computation of sound propagation through a turbofan engine inlet [1–4]. Relatively quiet modern turbofan engines rely heavily on acoustic treatment (liners) on the inlet wall [5].

As the design [5, 6] of treatment panels is laborious and expensive, their tests [7, 8] themselves can also be quite time consuming and costly, especially when broadband-frequency

0021-9991/98 $25.00
Copyright © 1998 by Academic Press
All rights of reproduction in any form reserved.

response is sought. Therefore, numerical techniques are often used to analyze sound propagation in lined ducts [7–10]. A time-domain method [11] is most suitable for the analysis of broadband-frequency problems.

Until recently only frequency-domain methods had been developed for the prediction of sound propagation in acoustically treated ducts [7], as well as for the extraction of the impedance property (inverse problem) of the material [9, 10]. This is because the development of time-domain impedance conditions had been hindered by the fact that the behavior of the lining material is frequency dependent [5]. In the past two years attempts [11, 12] were made toward the development of a time-domain impedance condition.

In 1996, inspired by the computational electromagnetics (CEM) community [13, 14], the present authors [11] used the z-transform to develop a numerically efficient time-domain acoustic impedance boundary condition. Starting from its standard frequency-domain counterpart [15] (particle displacement continuity), the authors formulated the impedance condition as only infinite-impulse-response (IIR) [16] type, digital filter operations, using the previous acoustic pressure and velocity information as well as the current acoustic velocity information in time. They demonstrated by one- and two-dimensional model problems that the developed boundary condition had potential promise for realistic applications.

In the same time frame, Tam and Auriault [12] addressed the stability of the standard formulation of the impedance condition. They claimed that, when applied in the solution of the linearized Euler equations in a uniformly moving medium, this boundary condition produces a convective instability (Kelvin–Helmholtz type). They attributed this instability to the existence of a vortex sheet used to simulate a narrow zero-velocity fluid layer adjacent to the wall as discussed by Tester [17]. However, their stability analysis was not consistent; the existence of the vortex sheet was not explicitly considered. Interestingly, the present authors used the same impedance condition with flow in the solution of the linearized Euler equations and observed stable solutions in the time domain. Supported by this and the inconsistency mentioned above, Tam and Auriault's stability analysis of the impedance condition is questionable.

It is the purpose of this paper to validate the developed time-domain impedance condition by solving an actual engineering problem. In particular, time-domain numerical simulations of the NASA Langley flow-impedance tube facility are performed both with and without flow. The simulations are carried out in two dimensions by solving the linearized Euler equations in the interior domain together with nonreflective conditions at the inlet and outlet boundaries of the test section and the time-domain impedance condition on the acoustically treated portion of the wall. The two-dimensional inflow boundary conditions of Giles [18] are used, together with a source condition to generate the incident waves at the desired frequencies and sound pressure levels, as well as to allow the passage of the outgoing waves without reflection at the source plane. Both single-frequency and broadband-frequency calculations are realized. It should be noted that this paper represents the first attempt to solve in the time domain an actual aeroacoustics problem with acoustic treatment.

Comparisons with experimental data reveal excellent agreement, especially at high frequencies, up to a flow Mach number of 0.3. This indicates that the present method is capable of producing the frequency-dependent response of the lining material accurately, despite the usage of a uniform mean flow assumption.

The mathematical development is described in the next section. First, the derivation of the time-domain impedance condition is summarized, and then the governing equations and nonreflecting boundary conditions are given. Next, the temporal and spatial discretizations

of the equations are discussed, and finally the results are presented and conclusions are drawn.

2. METHODOLOGY

2.1. Impedance Condition

A general form of the frequency-domain impedance condition was derived by Myers [15]. This derivation assumes that a soft wall (acoustically treated surface) undergoes small deformations about a mean stationary surface in response to an incident acoustic field from the fluid and this acoustic field is a small perturbation about a mean base flow. This boundary condition satisfies the continuity of particle displacement and is given, with an $e^{i\omega t}$ time dependence, assuming that the impedance has no spatial variation, as

$$i\omega\hat{p}(\omega,\mathbf{x})+\mathbf{V}_0(\mathbf{x})\cdot\nabla\hat{p}(\omega,\mathbf{x})-\mathbf{n}\cdot[\mathbf{n}\cdot\nabla\mathbf{V}_0(\mathbf{x})]\hat{p}(\omega,\mathbf{x})=-[i\omega Z(\omega)][\mathbf{n}\cdot\hat{\mathbf{V}}(\omega,\mathbf{x})], \quad (1)$$

where $\hat{p}$ is the complex amplitude of the pressure perturbation, $\hat{\mathbf{V}}$ is the complex amplitude of the velocity perturbation, $\mathbf{n}$ is the mean surface normal, ω is the circular frequency, Z is the impedance, and $\mathbf{V}_0$ is the mean velocity about which the linearization is performed. The impedance is a frequency-dependent complex quantity given by

$$Z(\omega)=R(\omega)+iX(\omega), \quad (2)$$

where $R(\omega)$ and $X(\omega)$ are the resistance and reactance, respectively, of the lining material. The impedance surface is assumed locally reacting [5, 19]; thus, the behavior of the lining material is independent of the surrounding.

Mathematically, the time-domain equivalent of the frequency-domain impedance condition given by Eq. (1) may be derived directly by taking its inverse Fourier transform. However, this results in a convolution integral whose evaluation requires long time histories of the normal velocity perturbation. Therefore, a straightforward implementation of the impedance condition in the time domain is impractical, especially for multidimensional problems.

The present authors [11] derived an efficient method for the implementation of the above impedance condition in time-domain algorithms using the z-transform and its time-shifting and convolution properties. The idea of using the z-transform comes from the impedance condition applications of the computational electromagnetics community [13, 14]. The development of the basic time-domain acoustic impedance condition was outlined by Özyörük and Long [11], giving examples of one-dimensional numerical and analytical solutions of a Gaussian pulse reflected off an acoustically treated wall. They showed excellent agreement between the computed and exact solutions. Here we summarize the basic method with an extension of its z-domain time-derivative operator to bilinear and second-order central difference approximations.

The two important properties of the z-transform [13, 16] are time-shifting and convolution, similar to the Fourier transform. If $q[n\Delta t]$ represents the nth time-discrete sample of the continuous variable $q(t)$, the time-shifting property is given by

$$\mathcal{Z}\{q[(n-1)\Delta t]\}=z^{-1}\mathcal{Z}\{q[n\Delta t]\}=z^{-1}Q(z), \quad (3)$$

where $\mathcal{Z}$ is the z-transform operator, and $Q(z)$ is the z-transform of $q[n\Delta t]$. The convolution

property is given by

$$\mathcal{Z}\{f[n\Delta t] * g[n\Delta t]\} = \mathcal{F}(z)\,\mathcal{G}(z), \tag{4}$$

where $f[n\Delta t] * g[n\Delta t]$ indicates the discrete convolution of functions f and g, and $\mathcal{F}(z)$ and $\mathcal{G}(z)$ are their z-transforms, respectively. A discrete convolution is an approximation to the continuous convolution of the exact formulation.

With the help of the time-shifting property (Eq. (3)) and with a first-order backward, or a second-order central difference, or a bilinear approximation a time derivative operator can be written in the z-domain as

$$i\omega \equiv \frac{\partial}{\partial t} \equiv \frac{1+\beta}{(1+\sigma)\Delta t}\,\frac{z^{\sigma} - z^{-1}}{1+\beta z^{-1}} = \mathcal{T}(z), \tag{5}$$

where $\beta = 0$ and $\sigma = 0$ for the first-order backward difference; $\beta = 0$ and $\sigma = 1$ for the second-order central difference; and $\beta = 1$ and $\sigma = 0$ for the bilinear approximation. The bilinear approximation is in general more accurate than the first-order backward difference [14].

Thus using Eqs. (4) and (5) the frequency-domain impedance condition (Eq. (1)) or the z-transform of its inverse Fourier transform may be written in the z-domain, suppressing the space dependence for brevity, as

$$\begin{aligned} &\frac{1+\beta}{(1+\sigma)\Delta t}\,\frac{z^{\sigma} - z^{-1}}{1+\beta z^{-1}}\,P(z) + [\mathbf{V}_0 \cdot \nabla - \mathbf{n} \cdot (\mathbf{n} \cdot \nabla \mathbf{V}_0)]P(z) \\ &\quad = -\frac{1+\beta}{(1+\sigma)\Delta t}\,\frac{z^{\sigma} - z^{-1}}{1+\beta z^{-1}}\,Z(z)\,V_n(z), \end{aligned} \tag{6}$$

where $P(z)$ and $V_n(z)$ are the z-transforms of the pressure and normal velocity perturbations, respectively, and $Z(z)$ is the z-transform of the impedance. This equation may be written as

$$[\mathcal{T}(z) + \mathcal{L}_s]P(z) = \mathcal{H}(z)\,V_n(z), \tag{7}$$

where $\mathcal{T}(z)$ is the time derivative operator given by Eq. (5), $\mathcal{L}_s$ is the spatial operator given by

$$\mathcal{L}_s = \mathbf{V}_0 \cdot \nabla - \mathbf{n} \cdot (\mathbf{n} \cdot \nabla \mathbf{V}_0) \tag{8}$$

and $\mathcal{H}(z) = -\mathcal{T}(z)\,Z(z)$. Thus $\mathcal{H}(z)$ of Eq. (7) can be thought of as the filter of the acoustic system, whose input and outputs are $V_n(z)$ and $[\mathcal{T}(z) + \mathcal{L}_s]\,P(z)$, respectively. Such a system produces stable outputs if the poles of $\mathcal{H}(z)$ are confined within the unit circle in the z-plane [16], provided that the input remains bounded.

Now let the z-transform of the impedance be modeled in general by

$$Z(z) = \frac{a_0 + \sum_{\ell=1}^{M_N} a_\ell z^{-\ell}}{1 - \sum_{k=1}^{M_D} b_k z^{-k}}, \tag{9}$$

where a's and b's are constant parameters that give the best approximation to the impedance data. Then, in order to obtain the time-domain impedance condition, we first substitute Eq. (9) into Eq. (6) and then multiply the resultant equation by $(1+\beta z^{-1})(z^{1-\sigma})$ and by the denominator of Eq. (9). Then rearranging and taking the inverse z-transform of the resultant equation we obtain

$$\frac{1+\beta}{1+\sigma}\,\frac{p^{n+1} - p^{n-\sigma}}{\Delta t} + \mathcal{L}_s\,p^{n+1-\sigma} = -a_0\,\frac{1+\beta}{1+\sigma}\,\frac{v_n^{n+1} - v_n^{n-\sigma}}{\Delta t} + R^{n,n-1,\cdots}, \tag{10}$$

where $\mathcal{L}_s$ is as defined by Eq. (8) and

$$R^{n,n-1,\cdots} = -\beta\,\mathcal{L}_s p^{n-\sigma} - \sum_{\ell=1}^{M_N} a_\ell \frac{1+\beta}{1+\sigma}\frac{v_n^{n+1-\ell} - v_n^{n-\sigma-\ell}}{\Delta t} + \sum_{k=1}^{M_D} b_k \left[\frac{1+\beta}{1+\sigma}\frac{p^{n+1-k} - p^{n-\sigma-k}}{\Delta t} + \mathcal{L}_s(p^{n+1-k-\sigma} + \beta p^{n-k-\sigma})\right] \quad (11)$$

in which p and v_n are the pressure and normal velocity perturbations on the wall, respectively, and the superscript n on a variable represents the nth time sample of the associated quantity. That is, $q[n\Delta t] \equiv q^n$. The latter is the assumed notation for the remaining discussion. Equation (10) is the general discrete-time-domain impedance condition and will be validated later with numerical simulations of the NASA Langley flow-impedance tube.

In general, the solution of Eq. (10) for the current time step acoustic pressure, p^{n+1}, requires the current time step acoustic velocity, v_n^{n+1}, and the acoustic pressure and velocity histories of lengths M_D and M_N, respectively, where M_D is the number of the constant b's, and M_N is the number of a's in the z-domain impedance model (Eq. (9)). The values of M_N and M_D vary depending on the frequency-dependent details of the impedance data. For a ceramic tubular liner, for example, used in this paper and as will be shown in the Appendix, M_N and M_D are 5 and 4, respectively. At this point it should be mentioned that the acoustic system is considered causal. In other words, acoustic perturbations are assumed absent for $t < 0$. This is a reasonable assumption since most CAA simulations start with a null acoustic field.

2.2. Modeling of Impedance

The impedance has to be modeled first in the z-domain in order to apply the above boundary condition in a numerical algorithm. The frequency-dependent behavior of the resistance and reactance must be provided accurately in the frequency range of interest. Substituting z^{-1} from Eq. (5) into Eq. (9), one can show that the resistance and reactance of the impedance must satisfy two equations of the forms, respectively,

$$\frac{R(\omega)}{\rho_0 c_0} = \frac{\tilde{a}_0 + \tilde{a}_1\omega^2 + \tilde{a}_2\omega^4 + \cdots}{\tilde{b}_0 + \tilde{b}_1\omega^2 + \tilde{b}_2\omega^4 + \cdots}, \quad (12)$$

$$\frac{X(\omega)}{\rho_0 c_0} = \frac{\tilde{c}_1\omega + \tilde{c}_2\omega^3 + \tilde{c}_3\omega^5 + \cdots}{\tilde{d}_0 + \tilde{d}_1\omega^2 + \tilde{d}_2\omega^4 + \cdots}, \quad (13)$$

where ρ_0 and c_0 are the ambient density and speed of sound, respectively, and $\tilde{a}$, $\tilde{b}$, $\tilde{c}$, and $\tilde{d}$ are constant parameters that give the best approximations to the actual resistance and reactance data. Notice that the resistance is an even function and the reactance is an odd function of the circular frequency ω. The reason for this is that when ω is substituted from Eq. (5) into the above models, the i dependence from the z-domain impedance is removed so that it becomes

$$Z(z) = R(z) + X(z). \quad (14)$$

Hence the corresponding a's and b's of Eq. (9) are easily identified.

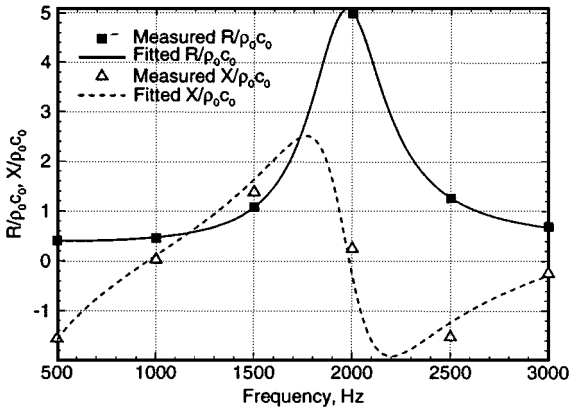

FIG. 1. Frequency-dependent resistance and reactance of a constant depth ceramic tubular liner (CT73).

The constant parameters of Eqs. (12) and (13) are not independent since their derivations start from Eq. (9). These parameters are found using a nonlinear least square fit (NLSF) algorithm based on the Levenberg–Marquardt method [20].

However, because of its rational form, there are some restrictions to the z-domain impedance function. For the stability [16] of the left-hand side of Eq. (7), the denominator of the impedance must not have zeroes outside the unit circle in the z-domain. Also for causality the region of convergence must be outside the outermost pole of $Z(z)$. These restrictions limit the flexibility of the NLSF procedure. Although, applying the NLSF method to Eqs. (12) and (13) independently, we found quite accurate resistance and reactance representations of the experimental impedance data used in this paper, these representations did not meet the stability and causality criteria. Somewhat less accurate but a causal and stable impedance function, shown together with the measured data in Fig. 1 for the ceramic tubular liner used in this paper, was obtained using the combination of low-pass, band-pass, etc. type filter functions,

$$\frac{Z(\omega)}{\rho_0 c_0} = r_1 + \frac{r_2 - r_1}{1 + i\omega r_3} + \frac{i\omega r_4}{(1 - \omega^2/r_6^2) + i\omega r_5} + i\omega r_7, \tag{15}$$

where the constants $r_{1,2,\ldots,7}$ were determined in an iterative manner ensuring that both the real and imaginary parts of the impedance were produced sufficiently accurately. Initial guesses of these parameters were crucial for the convergence of the NLSF iteration process. The final values of these parameters are given in the appendix for the data shown in Fig. 1. The z-domain equivalent of Eq. (15) can be found easily using the relation given by Eq. (5).

2.3. Governing Equations

The NASA Langley flow-impedance tube facility has a rectangular cross section with hard side walls (zero admittance). Plane waves are used as the acoustic source at the inlet and there is no mechanism to generate spanwise variations in the tube test section. Therefore, the numerical simulations are performed using the 2D linearized Euler equations, given here for completeness, in the Cartesian coordinate system with a uniform flow in the x-direction,

$$\frac{\partial \mathbf{Q}}{\partial t} + \frac{\partial \mathbf{E}}{\partial x} + \frac{\partial \mathbf{F}}{\partial y} = 0, \tag{16}$$

where $\mathbf{Q} = [\rho, u, v, p]^T$,

$$\mathbf{E} = \begin{Bmatrix} \rho_0 u + u_0 \rho \\ u_0 u + p/\rho_0 \\ u_0 v \\ u_0 p + \rho_0 c_0^2 u \end{Bmatrix}, \quad \mathbf{F} = \begin{Bmatrix} \rho_0 v \\ 0 \\ p/\rho_0 \\ \rho_0 c_0^2 v \end{Bmatrix} \tag{17}$$

in which ρ is the density perturbation, u is the velocity perturbation in the x-direction, v is the velocity perturbation in the y-direction, and p is the pressure perturbation, and the quantities with a zero subscript indicate the undisturbed quantities with c_0 being the speed of sound.

2.4. Nonreflecting Boundary Conditions

Calculations are performed on truncated computational domains using nonreflecting boundary conditions. The 2D nonreflecting boundary conditions of Giles [18] are used here. A source term is added to these conditions at the inflow boundary to generate an incoming train of acoustic waves to simulate the real situation in the flow-impedance tube. The test section of the tube is depicted in two dimensions in Fig. 2. This facility will be described later in Section 3.

The characteristics of the 2D linearized Euler equations are

$$\mathbf{Q} = \begin{Bmatrix} c_1 \\ c_2 \\ c_3 \\ c_4 \end{Bmatrix} = \begin{Bmatrix} p - c_0^2 \rho \\ \rho_0 c_0 v \\ p + \rho_0 c_0 u \\ p - \rho_0 c_0 u \end{Bmatrix}, \tag{18}$$

where c_1, c_2, c_3, and c_4 are associated with entropy waves, vorticity waves, and downstream and upstream running pressure waves, respectively. Nonreflecting boundary conditions are imposed for the c_1, c_2, and c_3 characteristics at the inlet (source plane), and the c_4 characteristic at the outlet. These boundary conditions are described below.

2.4.1. *Inflow Conditions*

The numerical simulations of the flow-impedance tube require that the inflow boundary allow the passage of both the incoming incident plane acoustic waves and the outgoing waves. The presence of the liner causes the generation of additional modes (nonplanar

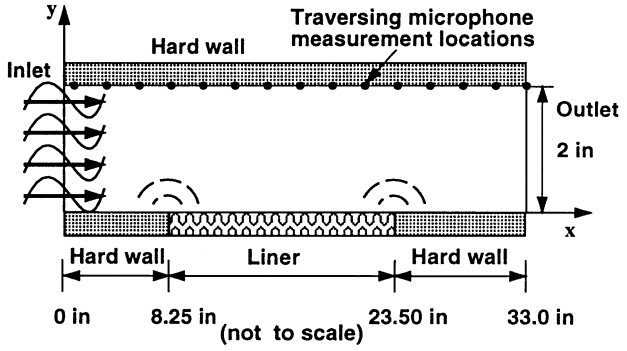

FIG. 2. 2D schematic of the test section of the NASA Langley flow-impedance tube.

waves) in the duct that can propagate in both directions, although they are expected to decay rapidly in the present configuration. The condition for the inlet boundary to be nonreflective, yet at the same time a source plane, is achieved by the addition of a source term to the boundary condition for the downstream running pressure wave (c_3), similarly to that of Hwang and Lee [21]. The complete set of equations at the inflow boundary is given by

$$\frac{\partial \mathbf{Q}_{\text{in}}}{\partial t} + \frac{\partial \mathbf{E}_{\text{in}}}{\partial x} + \frac{\partial \mathbf{F}_{\text{in}}}{\partial y} = \mathbf{S}_{\text{in}}, \tag{19}$$

where $\mathbf{Q}_{\text{in}} = \mathbf{Q}$ and are the characteristics given by Eq. (18) and

$$\mathbf{E}_{\text{in}} = \begin{Bmatrix} 0 \\ 0 \\ 0 \\ (u_0 - c_0)c_4 \end{Bmatrix}, \quad \mathbf{F}_{\text{in}} = \begin{Bmatrix} 0 \\ (c_0 + u_0)c_3/2 + (c_0 - u_0)c_4/2 \\ (c_0 - u_0)c_2/2 \\ c_0 c_2 \end{Bmatrix},$$

$$\mathbf{S}_{\text{in}} = \begin{Bmatrix} 0 \\ 0 \\ 2\sqrt{2}p_{\text{ref}}\, 10^{A/20}\omega\cos(\omega t) \\ 0 \end{Bmatrix}. \tag{20}$$

The source term on the right-hand side of the c_3 characteristic equation enables the creation of a plane wave at a circular frequency of ω and a sound pressure level (SPL) of A dB (p_{ref} is the reference pressure).

2.4.2. *Outflow Conditions*

The present simulations assume that there could not be reflections from the outlet boundary, although in real situations the impedance of the medium at downstream locations of the duct was measured to have both real and imaginary components. This indicates that in fact there exist reflections from downstream sections of the duct. This phenomenon is known to occur when the local conditions change (such as nonuniformities in the duct cross section and duct termination). However, the measured impedance values indicated these reflections were small. Therefore, they are ignored in this paper. To treat the outlet boundary conditions as nonreflective, 2D conditions are required since the additional modes could carry transverse velocity components downstream, especially when the outlet boundary is placed close to the liner trailing edge. The two-dimensional outflow condition of Giles given for the c_4 characteristic is used. The others are constructed from the interior equations. We present the complete set of equations for the outflow boundary in the same differential form as Eq. (19), with

$$\mathbf{Q}_{\text{out}} = \mathbf{Q}_{\text{in}}, \quad \mathbf{E}_{\text{out}} = \begin{Bmatrix} u_0 c_1 \\ u_0 c_2 \\ (u_0 + c_0)c_3 \\ 0 \end{Bmatrix}, \quad \mathbf{F}_{\text{out}} = \begin{Bmatrix} 0 \\ c_0(c_3 + c_4)/2 \\ c_0 c_2 \\ c_0 c_2 \end{Bmatrix}, \quad \mathbf{S}_{\text{out}} = 0. \tag{21}$$

In most situations here, it was found sufficient to set $c_4 = 0$ and to extrapolate the other characteristics from the interior. This is because the present configuration causes attenuation

of the nonplanar modes generated by the liner quickly. Results using both Eqs. (21) and this simpler form ($c_4 = 0$) will be shown later in Section 4.

The dependent perturbations at the inlet and outlet could be found from Eq. (18) by inversion after the solution of the boundary conditions for the characteristics:

$$\begin{aligned} \rho &= \left[-c_1 + \tfrac{1}{2}(c_3 + c_4) \right] / c_0^2, \\ u &= (c_3 - c_4)/2\rho_0 c_0, \\ v &= c_2/\rho_0 c_0, \\ p &= (c_3 + c_4)/2. \end{aligned} \tag{22}$$

2.5. Numerical Implementation

2.5.1. *Time Integration*

The four-stage, compact Runge–Kutta scheme is used for the time integration in this paper. For linear equations this method results in fourth-order time accuracy. If the semi-discretized time-dependent partial differential equations are given by

$$\frac{d\mathbf{Q}}{dt} = -[\mathcal{H}(\mathbf{Q}) - \mathcal{D}(\mathbf{Q})], \tag{23}$$

the R-K scheme is given by

$$\begin{aligned} \mathbf{Q}^{(0)} &= \mathbf{Q}^n, \\ \mathbf{Q}^{(s)} &= \mathbf{Q}^n - \alpha_s \Delta t \left[\mathcal{H}\left(\mathbf{Q}^{(s-1)}\right) - \mathcal{D}\left(\mathbf{Q}^{(0)}\right) \right], \\ \mathbf{Q}^{n+1} &= \mathbf{Q}^{(4)}, \end{aligned} \tag{24}$$

where $\mathbf{Q}$ is the vector of dependent solution variables, $\mathcal{H}(\mathbf{Q})$ is the collection of the spatial derivatives, $\mathcal{D}(\mathbf{Q})$ is artificial dissipation, and Δt is the time increment from one step to the next, and $\alpha_s = 1/4, 1/3, 1/2, 1$ for $s = 1, 2, 3$, and 4, respectively. Although artificial viscosity may deteriorate the results of long time integrations, it is required by the basic scheme to control nonphysical, high-frequency, background numerical oscillations. To minimize the effects of artificial dissipation, fourth- or sixth-order, low, constant-coefficient dissipation is used, depending upon the spatial discretization of the residuals $[\mathcal{H}(\mathbf{Q})]$. These will be discussed later.

For flat-wall boundary problems with a uniform mean flow $\mathbf{V}_0 = u_0 \hat{\mathbf{e}}_x$, $\mathcal{L}_s = u_0 \partial/\partial x$ and the time-discretized impedance boundary condition simplifies to

$$\frac{1+\beta}{1+\sigma} \frac{p^{n+1} - p^{n-\sigma}}{\Delta t} + u_0 \frac{\partial p^{n+1-\sigma}}{\partial x} = -a_0 \frac{1+\beta}{1+\sigma} \frac{v^{n+1} - v^{n-\sigma}}{\Delta t} + R^{n,n-1,\cdots}, \tag{25}$$

where

$$\begin{aligned} R^{n,n-1,\cdots} = &- \beta u_0 \frac{\partial p^{n-\sigma}}{\partial x} - \sum_{\ell=1}^{M_N} a_\ell \frac{1+\beta}{1+\sigma} \frac{v_n^{n+1-\ell} - v_n^{n-\sigma-\ell}}{\Delta t} \\ &+ \sum_{k=1}^{M_D} b_k \left[\frac{1+\beta}{1+\sigma} \frac{p^{n+1-k} - p^{n-\sigma-k}}{\Delta t} + u_0 \frac{\partial}{\partial x} (p^{n+1-k-\sigma} + \beta p^{n-k-\sigma}) \right]. \end{aligned} \tag{26}$$

This condition requires the full time step solutions p^{n+1} and v^{n+1} on the acoustically treated wall. The impedance condition states that there is transpiration of mass into or out of the wall. That is, no longer is $\mathbf{V}\cdot\mathbf{n}\neq 0$, as opposed to a hard-wall case. The amount of mass transpiration is fixed by the impedance of the wall. Therefore, instead of simple extrapolation of the density and the tangential velocities from the interior solution as in the case of a hard wall, we simply use the interior equations to solve for these quantities. The normal velocity in this case can also be solved using the interior equations. However, since the impedance condition has resulted in an implicit relation between the acoustic pressure and normal velocity on the wall, either the acoustic pressure or normal velocity at the current time level $n+1$ (full time step) must be provided by the flow solver. The other is obtained from the impedance condition. However, the application of the impedance condition in the R-K stages poses a difficulty because the intermediate solutions are advanced by fractions of the time step size. This is overcome by assuming that the acoustic velocity $v_n^{(s)}$ is the available value of v_n^{n+1} and this is then substituted into the impedance condition for v_n^{n+1} to obtain $p^{(s)}$ as the available value of p^{n+1} on the wall.

Thus the impedance condition may be rewritten, leaving the time-derivative operator switches β and σ intact, as

$$\frac{1+\beta}{1+\sigma}\left[\frac{p^{(s)}-p^{n}}{\alpha_s\Delta t}+\frac{p^{n}-p^{n-\sigma}}{\Delta t}\right]+(1-\sigma)u_0\frac{\partial p^{(s)}}{\partial x}=-\sigma u_0\frac{\partial p^{n}}{\partial x}$$

$$-a_0\frac{1+\beta}{1+\sigma}\left[\frac{v^{(s)}-v^{n}}{\alpha_s\Delta t}+\frac{v^{n}-v^{n-\sigma}}{\Delta t}\right]+R^{n,n-1,\cdots}, \tag{27}$$

where $R^{n,n-1,\cdots}$ is as given above. Note that in the case of $\beta=0$ and $\sigma=1$ the central time derivatives of the acoustic pressure and velocities are approximated by the average of two backward differences, taken at the R-K stage (s) and the time step n, respectively.

As mentioned earlier, the acoustic system is assumed to be causal. Therefore, the old time-derivative terms in the above equations are all zero to begin with, and they will be constructed as the time integration progresses. Now consider that the implicit pressure derivative term, i.e. $\partial p^{(s)}/\partial x$, is absent or $u_0=0$ (no flow) and the time derivative of the normal velocity is obtained from the R-K scheme explicitly (Eq. (24)). Then the time-discrete impedance condition can be rearranged to give

$$p^{(s)}=p^{n}-\alpha_s\Delta t\left[\mathcal{R}_1(p^{n,n-1,\cdots})+\mathcal{R}_2\left(v^{(s)}\right)+\mathcal{R}_3(v^{n,n-1,\cdots})\right], \tag{28}$$

where $\mathcal{R}_{1,2,3}(\,)$ are the collection of the remaining terms from Eq. (27). These terms will be of the same order of accuracy in time as the updated solution since they are basically composed of the old solutions and the current stage velocity solution from the R-K scheme. Therefore, Eq. (28) is nothing but an R-K update which will result in a fourth-order accurate integration of the acoustic pressure at the end of the time step. However, we found that the explicit solution of the normal velocity on a soft wall sometimes results in a numerical instability, even if there is no flow. The wall impedance is influential on this behavior. To circumvent the stability problem and account for the fact that the impedance condition contains an implicit pressure derivative term from its inception, we discretize the normal momentum equation implicitly in pressure as well. In this case, we no longer possess higher-order accuracy in the integration of the impedance condition. Of course, high-order schemes are desirable in CAA, but this is the exchange one has to make for stable solutions.

Nevertheless, we believe relatively more accurate than first-order results may be obtained with the current time-integration approach, because of its multistage nature and use of the acoustic velocity from the R-K scheme.

Now, as we mentioned, the normal momentum equation is discretized semi-implicitly (implicit in pressure derivative) within an R-K stage (s) and its simultaneous solution with Eq. (27) is performed. The time-discretized normal momentum equation is given by

$$\frac{v^{(s)} - v^n}{\alpha_s \Delta t} + u_0 \frac{\partial v^{(s-1)}}{\partial x} + \frac{1}{\rho_0} \frac{\partial p^{(s)}}{\partial y} = \mathcal{D}\big(v^{(0)}\big). \tag{29}$$

Although it may seem that taking the $\partial p/\partial y$ derivative in the normal momentum equation at the current R-K stage (s) rather than the previous stage would require an implicit solution in the entire computational domain, the interior solution is performed explicitly and made available prior to the application of the impedance boundary condition. Hence the implicit characteristics of the impedance condition and the normal momentum equation are confined only on the soft wall where they are being applied. The semi-implicit discretization of the momentum equation enhances numerical stability, as was also shown with one-dimensional example calculations in Ref. [11].

2.5.2. *Spatial Discretization*

The substitution of Eq. (29) into Eq. (27) is made to eliminate $v^{(s)}$ from the impedance condition,

$$\begin{aligned} p^{(s)} + (1-\sigma^2)\frac{\alpha_s \Delta t u_0}{1+\beta}\frac{\partial p^{(s)}}{\partial x} - \frac{a_0 \alpha_s \Delta t}{\rho_0}\frac{\partial p^{(s)}}{\partial y} &= p^n - \alpha_s (p^n - p^{n-\sigma}) \\ - \sigma(1+\sigma)\frac{\alpha_s \Delta t u_0}{1+\beta}\frac{\partial p^n}{\partial x} + a_0 \alpha_s \Delta t \left[u_0 \frac{\partial v^{(s-1)}}{\partial x} - \mathcal{D}\big(v^{(0)}\big) - \frac{v^n - v^{n-\sigma}}{\Delta t} \right] \\ + (1+\sigma)\frac{\alpha_s \Delta t}{1+\beta} R^{n,n-1,..}, \end{aligned} \tag{30}$$

where $R^{n,n-1,\cdots}$ is as given by Eq. (26). Note that some of the terms in these equations vanish when the values of β and σ (0 or 1) are substituted.

Although Eq. (30) has now only $p^{(s)}$ as an unknown, its solution is a significant issue in the case of flow and $\sigma = 0$. When this equation is discretized in space with $\sigma = 0$, the result is a linear system of equations arising from the $u_0 \partial p^{(s)}/\partial x$ term. For a fully three-dimensional problem, this term is equivalent to the product of the tangential gradient of the acoustic pressure and the mean tangential velocity on the wall. The impedance condition is applied at every R-K stage, and therefore, the linear system of equations (space-discretized form of Eq. (30)) has to be inverted at every R-K stage to determine the wall pressure perturbation $p^{(s)}$. Then the velocity perturbation $v^{(s)}$ is found conveniently from Eq. (27) or Eq. (29). As mentioned earlier this process has to be preceded by the solution of the interior and hard-wall points so that the linear system of equations is closed with the field information from the outside of the soft-wall.

Second- or fourth-order accurate spatial discretization (central in the interior and biased at or near the boundaries) is used in both the x and y coordinates for the solution of the flow-impedance tube problem. In most cases here the length of the test section of the tube

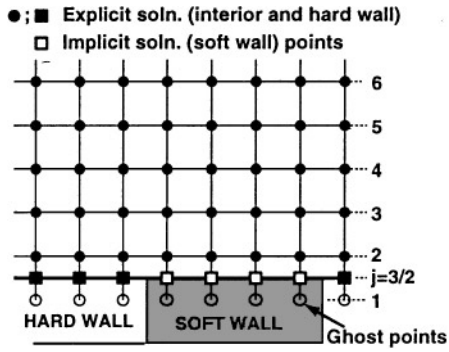

FIG. 3. Spatial discretization at and near the wall.

is only several wavelengths at the highest of the considered frequencies; and therefore, we will easily have sufficient resolution (number of grid points for wavelength, NPPW) to use only second-order discretization.

Constant mesh spacings (Δx and Δy) are used in both the x and y directions. The wall is placed halfway between two grid points, allowing a ghost grid point inside the wall, as shown in Fig. 3. This permits the proper discretization of the equations since there exist both incoming and outgoing waves at a soft-wall boundary, as opposed to a solid wall. In flow cases, the second-order spatial discretization of the impedance condition results in a tri-diagonal equation system and the fourth-order discretization results in a penta-diagonal equation system. Discretizing this equation on the wall ($j = 3/2$) yields an equation system in the unknown wall ghost point acoustic pressure in general,

$$A_i\, p^{(s)}_{i-2,1} + B_i\, p^{(s)}_{i-1,1} + C_i\, p^{(s)}_{i,1} + D_i\, p^{(s)}_{i+1,1} + E_i\, p^{(s)}_{i+2,1} = RHS_i, \tag{31}$$

where the subscript i signifies the grid point index in the x direction. For the second-order discretization A_i and E_i are zero (tri-diagonal equation system). For the no-flow case or $\sigma = 1$, A_i, B_i, D_i, and E_i are all zero, and $p^{(s)}_{i,1}$ is simply given by $p^{(s)}_{i,1} = RHS_i / C_i$.

In obtaining the above linear system of equations the wall pressure was assumed to be given by an interpolation formula. In fact, any quantity at the wall is found from

$$q_{i,3/2} = \phi_1 q_{i,1} + \phi_2 q_{i,2} + \phi_3 q_{i,3} + \phi_4 q_{i,4}, \tag{32}$$

where $q_{i,1}$ is the ghost point quantity inside the wall (Fig. 3). For the second-order case $\phi_1 = 1/2, \phi_2 = 1/2, \phi_3 = 0$, and $\phi_4 = 0$. For the fourth-order case $\phi_1 = 5/16, \phi_2 = 15/16$, $\phi_3 = -5/16$, and $\phi_4 = 1/16$.

As mentioned earlier, fourth-order dissipation is used with the second-order calculations of the residuals, and sixth-order dissipation is used with the fourth-order calculations. The fourth- and sixth-order dissipation is given, respectively, by

$$\mathcal{D}^{(4)}(\mathbf{Q}) = -\frac{\kappa^{(4)}}{\Delta t}\left(\delta_x^4 + \delta_y^4\right)\mathbf{Q}, \quad \mathcal{D}^{(6)}(\mathbf{Q}) = \frac{\kappa^{(6)}}{\Delta t}\left(\delta_x^6 + \delta_y^6\right)\mathbf{Q}, \tag{33}$$

where $\delta_x^4 \mathbf{Q}|_{i,j} = \sum_{r=-2}^{2} w_r \mathbf{Q}_{i+r,j}$ with $w_r = [1, -4, 6, -4, 1]$ for $r = -2, \ldots, 2$ and, similarly, $\delta_x^6 \mathbf{Q}|_{i,j} = \sum_{r=-3}^{3} w_r \mathbf{Q}_{i+r,j}$ with $w_r = [1, -6, 15, -20, 15, -6, 1]$ for $r = -3, \ldots, 3$,

respectively. The y-direction operators are defined similarly. Dissipation is set to zero if a value beyond a boundary is needed. Typical values of the constants $\kappa^{(4)}$ and $\kappa^{(6)}$ are $1/128$ and $1/512$, respectively.

3. EXPERIMENTAL SETUP

Two test specimens were used in the current investigation. The first was a hard-wall specimen. Since the results for this configuration are well understood, this provided a useful check for the current analytical procedure. The second test specimen was constructed with ceramic tubular material, which consists of a large number of $\frac{1}{40}$-inch diameter parallel tubes. The open cell porosity and total depth of this liner are 57% and 3 in, respectively. This material is very useful for laboratory studies [7] because of its consistent properties which can be described well analytically. Also, changes in the impedance of the ceramic tubular material due to grazing flow effects are relatively minor. The frequency-dependent impedance of this material is plotted in Fig. 1.

The input data used to extract the impedance of the test specimen was obtained from measurements using a flow-impedance tube in the NASA Langley Flow-Impedance Test Laboratory [7]. This multiconfigurational apparatus is designed to produce a controlled aeroacoustic environment with a flow speed of up to Mach 0.6 over a test specimen length of up to 16 in. Four 120-W, phase-matched acoustic drivers generate signals over a frequency range of 0.3 to 3.0 kHz, with sound pressure levels up to 160 dB at the test specimen leading edge.

The current study was conducted with a test specimen length of 15.25 in and with SPL of 130 dB at each frequency of interest at the source plane. A schematic of the flow-impedance tube test section is provided in Fig. 2. The side walls and the upper wall have zero admittance throughout the test section. This section is approximately 33 in long, with a 2-in by 2-in cross section. Acoustic plane waves are propagated down the tube (left to right in the figure), across the surface of the test specimen, and into a termination section designed to be very nonreflective over the frequency range of interest (0.5 to 3.0 kHz). An 0.5-in wide precision-machined slot in the top wall of the flow-impedance tube allows an axial traverse bar to traverse the test section length by means of a digital stepping motor under computer control.

At each test frequency, a pure tone sound pressure level was set at the source plane. Acoustic pressure measurements were acquired with the traversing microphone (mounted in the axial traverse bar) at a number of selected measurement locations from 8.25 in upstream of the leading edge of the test specimen to 0.75 in downstream of the trailing edge of the test specimen.

4. DISCUSSION OF SIMULATIONS

The results are discussed in this section. The numerical simulations are performed and compared with experimental data for a frequency range of 0.5 to 3.0 kHz with 0.5 kHz increments and at mean-flow centerline Mach numbers of 0.0, 0.1, 0.3, and 0.5. In the experiments with Mach numbers higher than 0.5, very strong reflections occurred from the downstream terminating section of the duct and as a result no data was measured. Therefore, we do not attempt to perform numerical simulations for $M > 0.5$. As mentioned earlier, changes to the impedance of the ceramic tubular material due to grazing flow effects are relatively minor. For convenience, therefore, the same impedance data are used at all Mach numbers.

Before discussing the results it is useful to describe the analytical impedance functions used for the calculations. Both single-frequency and broadband-frequency computations are carried out for investigating the effects of various parameters on the solutions and for validating the present method against experimental data. Depending upon the acoustic source and the impedance function, the simulations are denoted either single-frequency simulations A (or B) or broadband-frequency simulations, as described below:

1. *Single-frequency simulations A.* This set of simulations uses an assumed impedance function of the form

$$\frac{Z(\omega)}{\rho_0 c_0} = R_0 + i\omega\, a + b/i\omega, \tag{34}$$

where R_0 is the specific resistance, and a and b are two adjustable parameters to obtain the correct reactance at the specified frequency. This form of the impedance function is useful for single-frequency runs simulating the exact (experimental) impedance property. The z-domain equivalent of this impedance function, which will be referred to as the single-frequency impedance function and denoted by $Z_S(z)$ here, is obtained easily by the substitution of Eq. (5) for the $i\omega$ term above. Although only the first-order backward difference ($\beta = 0, \sigma = 0$) is used for $i\omega$ in the impedance function, we obtain solutions using the backward, central difference, and bilinear approximations for the time derivative term in the impedance condition itself.

2. *Single-frequency simulations B.* The second set uses the impedance function from the nonlinear least square fit applied to Eq. (15). The resultant curves are shown in Fig. 1. Although the resistance is represented quite well, the reactance is somewhat inaccurate at some frequencies. Table 1 in the Appendix compares quantitatively the fitted impedance values with the data. The resultant z-domain impedance function, which will be referred to as the broadband-frequency impedance function and will be denoted by $Z_B(z)$ here, has poles inside the unit circle but they are extremely close to it (see Appendix for $Z_B(z)$). It will be shown below that the predicted SPLs are somewhat sensitive to the slight differences between the experimental data and approximate impedance values. This set of runs is also performed for each frequency individually. Therefore, the only difference between the previous set of runs and this set is due to the impedance function $Z(z)$ used.

3. *Broadband-frequency simulations.* Finally in the third set of runs, all the frequencies are run at once using the impedance function $Z_B(z)$. A fast Fourier transform (FFT) is performed to the time-accurate solution to obtain the SPLs for each individual frequency. For this the source term of the inflow boundary condition is replaced by

$$2\sqrt{2}\, p_{\text{ref}}\, 10^{\text{SPL}/20} \sum_{m=1}^{6} (m\omega_0) \cos[m\omega_0 t + (m-1)\pi/3],$$

where SPL = 130 dB, and $\omega_0 = 2\pi f_0$ with $f_0 = 500$ Hz. This set of runs is significant to show how one can solve broadband-frequency problems with only a single computer run, using the present time-domain impedance condition.

In the following discussions, the SPL is calculated from

$$\text{SPL} = 20 \log_{10}(p_{\text{rms}}/p_{\text{ref}}); \quad p_{\text{rms}}^2 = \frac{1}{t_2 - t_1} \int_{t_1}^{t_2} p^2(t)\, dt. \tag{35}$$

A trapezoidal integration rule is used to calculate the root-mean-square (rms) pressure, p_{rms}, numerically. The data required by this equation are collected after the transients leave the computational domain and the field becomes periodic.

4.1. Effects of Various Parameters

First, the ability to generate plane waves at the specified SPL using the present inflow conditions is tested at various operating conditions without the liner present. These tests use a Courant number (CFL) of 0.5 and a grid resolution of 23 points per wavelength (PPW) in the upstream direction and 32 PPW in the normal direction for the highest frequency (3.0 kHz). The CFL number is defined by $\text{CFL} = \Delta t[(u_0 + c_0)/\Delta x + c_0/\Delta y]$. The simple $c_4 = 0$ characteristic boundary condition is imposed at the outlet with a second-order spatial discretization of the interior and inflow boundary condition equations.

Figure 4 shows the SPLs along the upper wall for two sets of extreme operating conditions of the simulated cases in this paper. It is evident from the figure that the inlet boundary conditions generated the plane waves at the desired SPL (130 dB). The outlet boundary conditions caused only insignificant reflections. Although the pressure levels appear to be very oscillatory, the scale of the vertical axis should be noted. In fact, the reflected waves caused only a 0.25 dB fluctuation at the worst case, and this was only near the outlet boundary.

Since the liner causes additional modes to be generated in the impedance tube, it is important to characterize the behavior of the inflow and outflow conditions against more complicated sound fields. This is realized using three different size domains with a broadband-frequency source (0.5 to 3.0 kHz with 0.5 kHz increments) and a $M = 0.1$ flow with a liner extending from 8.25 to 23.5 inches on the lower wall. Fourth-order spatial discretization is employed in both the x and y directions with a bilinear time discretization ($\beta = 1$, $\sigma = 0$) for the impedance condition. The computations are carried out on meshes with a resolution of approximately $\text{NPPW}_x = 22.7$ and $\text{NPPW}_y = 26.7$ at 3.0 kHz and using a CFL of 0.64.

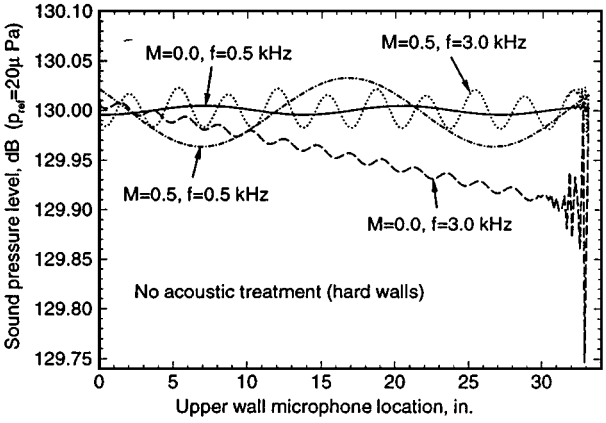

FIG. 4. Test of the acoustic source at various operating conditions without acoustic treatment. $\text{NPPW}_x = 23$, $\text{NPPW}_y = 32$ at 3.0 kHz, and $\text{CFL} = 0.5$. Second-order discretization and 1D outflow condition used.

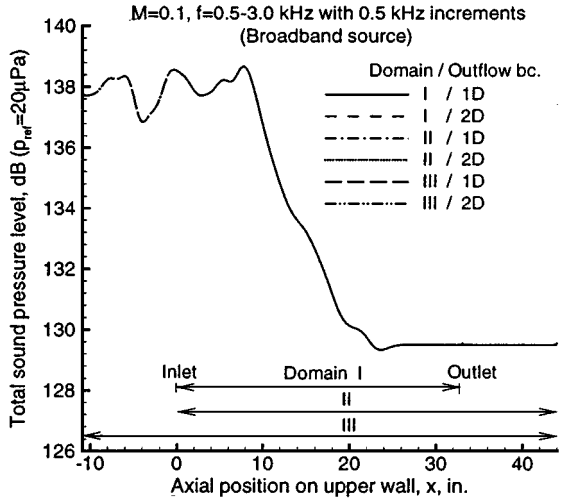

FIG. 5. Test of the inflow and outflow boundaries in the presence of a liner extending from $x = 8.25$ to 23.50 in. $M = 0.1$, $f = 0.5$–3.0 kHz with 0.5 kHz increments, CFL $= 0.64$ ($\Delta t = 1/512\, f_0$, $f_0 = 0.5$ kHz), $\text{NPPW}_x = 22.7$, $\text{NPPW}_y = 26.7$ (at 3.0 kHz). Fourth-order spatial discretization and $\beta = 1$, $\sigma = 0$ used.

Figure 5 indicates the locations of the reference source planes (inlet) and outlet boundaries and shows the resultant total SPLs using both the 2D outflow condition and the simple $c_4 = 0$ characteristic boundary condition (denoted as 1D in the figure). In all cases the total SPL curves overlap each other in the extend of the shortest domain and their transitions beyond are very smooth. This indicates that both the inflow and outflow boundary conditions work very well for the present configuration and frequency range of interest. Therefore, we choose the source plane to be at $x = 0$ and outlet boundary at $x = 33$ in, as illustrated in Fig. 2, for the rest of the calculations.

The effects of the spatial discretization on the accuracy of the solutions in the present simulations are also investigated using the same acoustic source and resolution parameters as those used in the previous test. The results are shown in Fig. 6 for the total SPL on the upper wall. Although low-order schemes possess higher numerical diffusion and dispersion rates, the solutions yielded by both the second- and fourth-order schemes agree perfectly, owing to the use of sufficient grid points per wavelength. Since the waves propagate only several wavelengths (at the highest frequency) before they leave the computational domain and consequently numerical errors will not accumulate considerably, we usually employ at least 20–25 PPW to obtain adequate results with the second-order scheme. For longer domains, or in the case of reflections from the outlet boundary (complex impedance), more grid points per wavelength will be needed to retain accuracy because the waves will remain in the domain longer. The NPPW requirement for the fourth-order scheme may be relaxed to about 15–20.

The final numerical test concerns the effects of the temporal resolution (CFL) and the time discretization (β, σ) of the impedance condition on the solutions. For this a single-frequency simulation at a frequency of 0.5 kHz and flow Mach number of 0.1 is performed. A 188×14 grid is used ($\text{NPPW}_x = 136$ and $\text{NPPW}_y = 160$). Fourth-order spatial discretization is employed to keep the spatial discretization errors to the lowest levels possible.

Figure 7 shows the SPLs on the upper wall at various CFL numbers ranging from 0.64 to 0.08 with both $\beta = 0, \sigma = 0$ and $\beta = 1, \sigma = 0$. The calculations using the central time

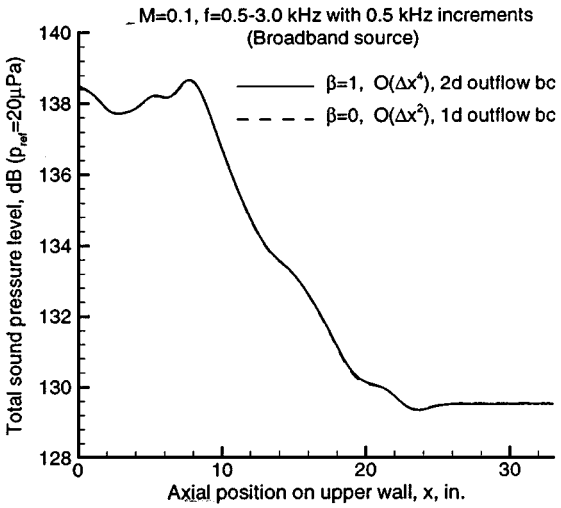

FIG. 6. Effects of the spatial discretization on the solution. $M = 0.1,\ f = 0.5$–3.0 kHz with 0.5 kHz increments, CFL $= 0.64$ ($\Delta t = 1/512\, f_0,\ f_0 = 0.5$ kHZ), NPPW$_x = 22.7$, NPPW$_y = 26.7$ (at 3.0 kHz).

difference in the impedance condition (i.e., $\beta = 0, \sigma = 1$) became unstable because of the flow. Therefore, no results are presented with the central time difference. Sound pressure levels were calculated integrating the solution over 10 wave periods. It appears that the time step size and the choice of β affect the solutions only negligibly.

It should be noted at this point that because of the reinforcement of the downstream traveling sound waves by the upstream traveling waves, the SPL at the reference source plane is perturbed from what we set (130 dB) for the incoming waves. This can be seen in Fig. 7. In experiments the reference plane SPL (which is due to both the incoming and outgoing waves) can be measured and fed to the sound-generating speakers so that necessary adjustments can be made to attain a 130-dB SPL. However, in the numerical implementation

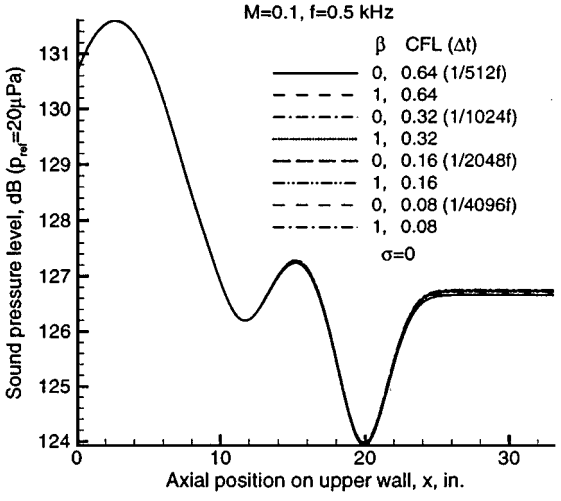

FIG. 7. Effects of the time discretization of the impedance condition and the time step size of the R-K integration on the solution. $M = 0.1,\ f = 0.5$ kHz, NPPW$_x = 136$, NPPW$_y = 160$. Fourth-order spatial discretization used.

it is not convenient to do this and any deviations to the experimental SPL at the reference plane are subtracted from the solution so that the numerical results can be compared with experiments in the same norms.

4.2. Comparisons with Experiment

After establishing the effects of various parameters, we now perform an extensive numerical study of the flow-impedance tube with comparisons to experiment. As mentioned earlier, simulations are performed at mean-flow centerline Mach numbers of 0.0, 0.1, 0.3, and 0.5, using both the single-frequency and broadband-frequency sources.

We first present Fig. 8 to illustrate how the overall sound field looks in the impedance tube at each particular frequency of interest. These results were obtained at $M = 0.1$ using the single-frequency impedance function and $\beta = 0$, $\sigma = 0$. Because of the frequency-dependent response of the liner, the pressure levels are seen to differ substantially as the frequencies of the incident waves are changed. The most attenuation is obtained at 1.0 kHz (near resonant frequency). It will be shown below that as the flow Mach number is changed the details of the upper wall SPL remain similar but the attenuation rates and levels change considerably.

4.2.1. *No-Flow Case*

The simulations for the no-flow case were performed with $\beta = 0$, $\sigma = 0$ and second-order spatial discretization on a 188×14 grid with a resolution of $\text{NPPW}_x = 25$ and $\text{NPPW}_y = 26$ for the highest frequency (3.0 kHz). Both the broadband-frequency simulation (BFS) and single-frequency simulations A (SFS-A) and B (SFS-B) were performed. A CFL of 0.5 was used for the SFS-A and SFS-B and a CFL of 0.7 was used for the BFS. An FFT was applied to the broadband solution to extract the SPL for each frequency of interest while the SPLs of the single-frequency cases were found from Eq. (35).

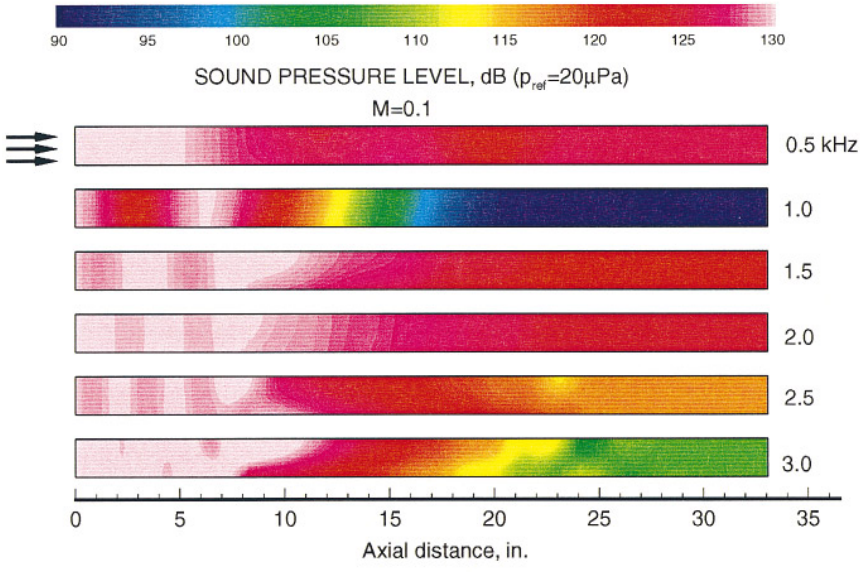

FIG. 8. Time-domain numerical simulation of the NASA Langley flow-impedance tube with a constant depth ceramic tubular liner. Sound pressure level contours are illustrated for each frequency at the $M = 0.1$ flow condition.

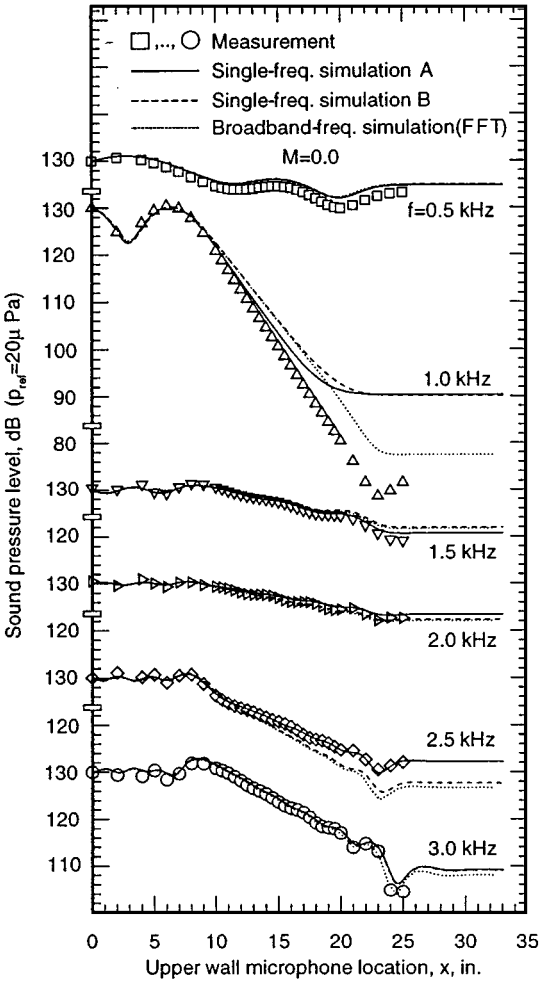

FIG. 9. Upper wall SPLs given by the single- and broadband-frequency simulations (SFS-A/B and BFS). $M = 0.0$, CFL $= 0.5$ for SFS-A/B and CFL $= 0.64$ for BFS. Second-order discretization and $\beta = 0$, $\sigma = 0$ used. Lowest $\text{NPPW}_x = 25$.

Figure 9 shows the comparison of the upper wall SPL results of the current calculations with the measured data. The solid, dashed, and dotted lines represent the SFS-A, SFS-B, and BFS, respectively. The symbols indicate the experimental data. The agreement between the measurements and the current results is excellent in general, except at 1.0 kHz. The discrepancies seen at some frequencies, especially at 2.5 kHz, between the SFS-A and SFS-B results are due to the differences between the reactance values the impedance functions $Z_S(z)$ and $Z_B(z)$ produced at these frequencies. The sensitivity of the results to the perturbations in the impedance data is sometimes a function of the sound field we are working with. This is probably the case we have here; and therefore, there is a need to improve the functional representation of the impedance for broadband calculations. This could be done using more terms in the z-domain impedance model. This, however, was not realized in the present study.

Also, an interesting situation occurs when the results of the SFS-B and BFS are compared. These cases both used the impedance function $Z_B(z)$, and the SPLs corresponding

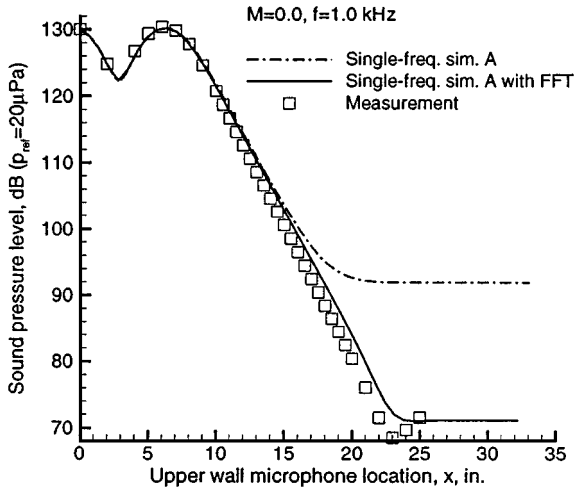

FIG. 10. Single-frequency solution at 1.0 kHz with and without FFT at $M = 0.0$.

to them were expected to be identical. Obviously this is not the case for some frequencies, particularly for 1.0 kHz. Since the BFS results for each frequency were identified through an FFT, these discrepancies suggest that, especially at 1.0 kHz, the single-frequency results contained some low amplitude harmonics or some mean component to the acoustic pressure and this contributed to the SPLs calculated directly using Eq. (35). This is also evidenced by the SFS-B result for 1.0 kHz. To support this we also applied an FFT to the SFS-A solution at this frequency. Figure 10 shows and compares to experiment the SFS-A results with and without FFT. Now the current simulation at 1.0 kHz also agrees with the experimental data perfectly. The discrepancy was in fact being caused by approximately two orders of magnitude lower mean pressure than the source, as shown in Fig. 11, as the zero frequency

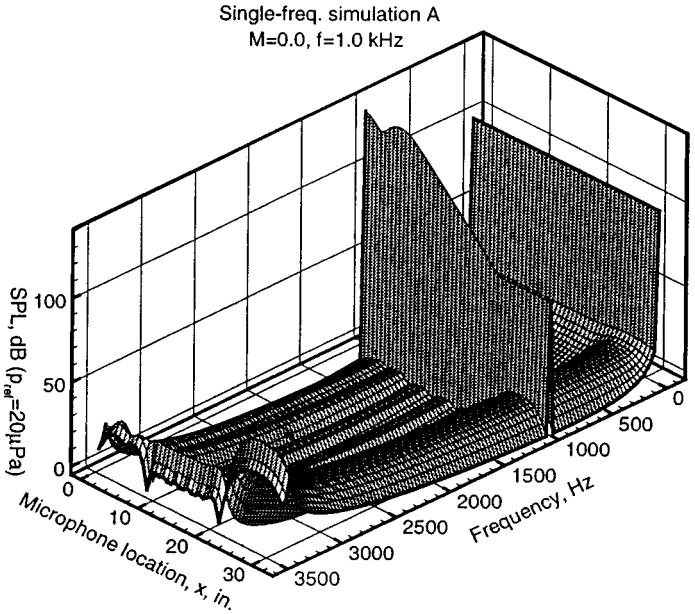

FIG. 11. Existence of a very low, nonzero mean (peaked at 0.0 kHz) along the entire test section at 1.0 kHz and $M = 0.0$.

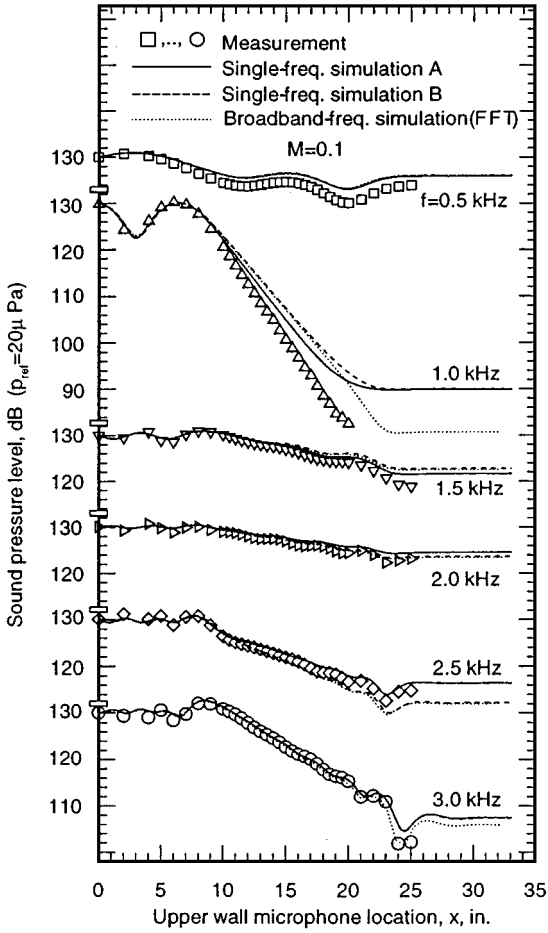

FIG. 12. Upper wall SPLs given by the single- and broadband-frequency simulations (SFS-A/B and BFS). $M = 0.1$, CFL $= 0.5$ for SFS-A/B and CFL $= 0.64$ for BFS. Second-order discretization and $\beta = 0, \sigma = 0$ used. Lowest $\text{NPPW}_x = 22$.

component of the FFT results. This figure reveals that the mean pressure existed along the entire tube, which was not accounted for in the rms calculation using Eq. (35).

4.2.2. $M = 0.1$ *Case*

The simulations for the $M = 0.1$ case used the same resolution, time, and space discretization parameters as the no-flow case, except the NPPW_x was reduced to 22 because of the flow effects. The same sets of simulations (SFS-A, SFS-B, and BFS) as the no-flow case were performed.

Figure 12 shows and compares the results with the measurements. Although similar trends are observed in the results, a close inspection of these results and the comparisons of the no-flow case indicate that the background flow caused some relative shifts from the experiment toward higher SPLs. However, these deviations are minor at this Mach number. The agreement between the current results and the measurements is again excellent, except near the resonant frequency. As has been shown above, however, the existence of a nonzero mean pressure along the tube applies also to this case.

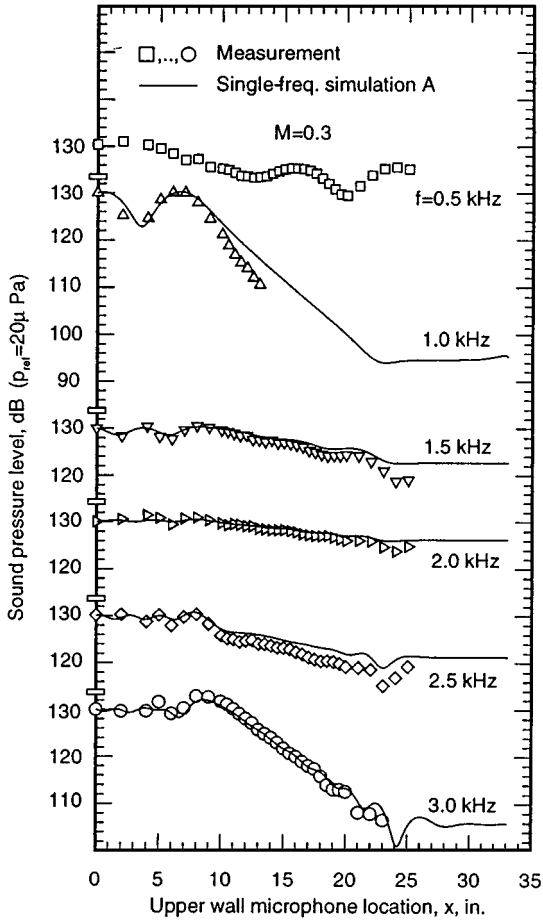

FIG. 13. Upper wall SPLs given by the single-frequency simulations. $M = 0.3$, CFL $= 0.5$. Second-order discretization and $\beta = 0, \sigma = 0$ used. Lowest $\text{NPPW}_x = 23$.

4.2.3. $M = 0.3$ *Case*

Only SFS-A were performed at $M = 0.3$. The same size mesh as the previous two cases was used for the frequencies up to 2.0 kHz and a 252×14 mesh was used for the 2.5 and 3.0 kHz cases, giving a lowest spatial resolution of $\text{NPPW}_x = 23$ and $\text{NPPW}_y = 26$. A CFL of 0.5 was used for all frequencies. The second-order scheme with $\beta = 0, \sigma = 0$ was employed.

The comparisons in Fig. 13 reveal that the computations again captured the details of the upper wall SPL very well, but generated some increased deviations from experiment. In other words, compared to the experimental data, increased differences in the attenuation rates are observed as the flow Mach number is increased. As will be shown for the $M = 0.5$ case, this is mainly due to our usage of the peak values from the measured background mean-flow velocity profiles. An improvement is observed when averaged values are used.

Notice in Fig. 13 that no results are presented at 0.5 kHz. This is because we encountered numerical instabilities at this frequency. These instabilities arose in the transitional regions between the soft and hard walls (leading and trailing edge regions of the liner), merely

due to the infinitely large jumps in the impedance data. It should be noted that the use of a 188×14 grid resulted in a mesh resolution of $\text{NPPW}_x = 106$ and $\text{NPPW}_y = 160$ for this particular frequency and consequently lack of dissipation. Therefore, it was extremely difficult to control the development of spurious waves.

The broadband simulations (BFS) at $M = 0.3$ also failed for the same reason. The mesh was constructed to resolve the highest frequency (3.0 kHz) with at least $\text{NPPW}_x = 23$ and $\text{NPPW}_y = 26$ and, on the other hand, this meant six times more grid points for the 0.5 kHz components of the waves. Therefore, it became impossible to suppress the spurious waves, and no solutions could be attained. The existence of a wide range of frequencies in a problem is a major obstacle for numerical methods in terms of resolving them equally.

Two attempts were made to alleviate the stability problem. The first included the incorporation of a spatial variation into the leading term (resistance) of the single-frequency impedance function so that a smooth transition could be made from the soft wall to the hard wall via increased resistances. A half-Gaussian function was used as a resistance scale and to account for this necessary modifications were made to the impedance condition analytically.

This, however, worsened the situation; instabilities developed more rapidly. Perhaps we needed to incorporate a spatially changing reactance to remove its discontinuity as well. However, this would bring a considerable amount of complications to the formulations of the present method. This is considered for future work.

The second partially successful attempt was to reduce the grid resolution and to perform only a 0.5 kHz single-frequency computation. For this, the spatial resolution in the x direction was reduced by a factor of $2/3$, still with sufficient NPPW. Although this prevented instabilities from growing further, we still had shock-like short-wave components in the solution in the vicinity of the liner leading (LE) and trailing edges (TE) as illustrated in Fig. 14 at increasing times. These shock-like spurious waves grew and shrank statically (i.e., without propagating in x), especially in the TE region, as the axial gradient of the acoustic pressure changed. Figure 15 shows the resultant upper wall SPLs together with the measured data. The agreement is not as good in terms of the details of the SPL on the upper

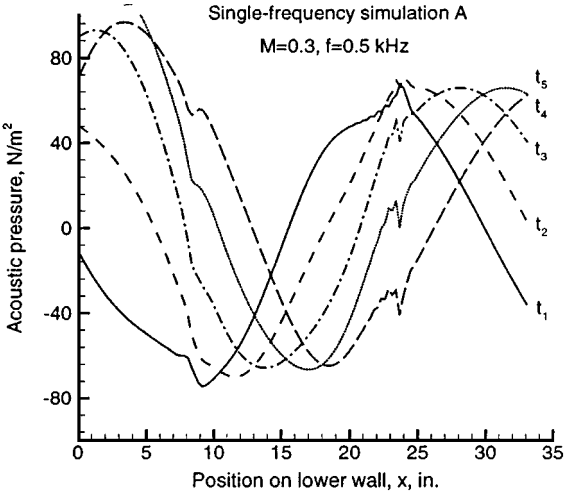

FIG. 14. Lower wall pressure: shock-like spurious waves at the LE and TE of the liner. $M = 0.3$ and $f = 0.5$ kHz. $\text{CFL} = 0.6$, $\text{NPPW}_x = 69$ and $\text{NPPW}_y = 160$. Second-order discretization and $\beta = 0$, $\sigma = 0$ used.

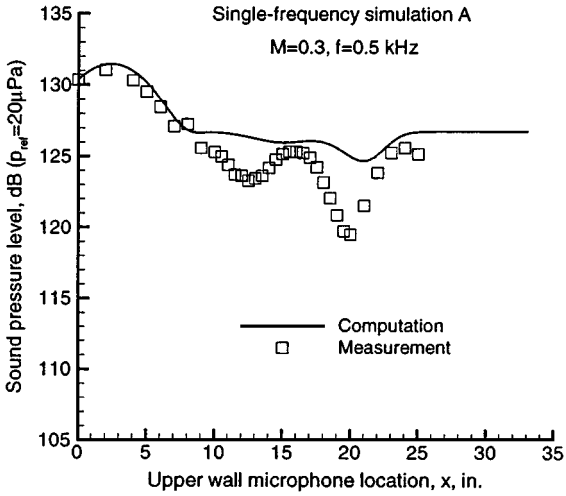

FIG. 15. Upper wall SPL at $M = 0.3$ and $f = 0.5$ kHz. CFL $= 0.6$, NPPW$_x = 69$, and NPPW$_y = 160$. Second-order discretization and $\beta = 0$, $\sigma = 0$ used.

wall. We think that those spurious waves are responsible for the degradation of the results, in addition to the unaveraged mean flow effects.

4.2.4. $M = 0.5$ *Case*

At the $M = 0.5$ flow condition only the 2.5-kHz SFS-A could be performed. A mesh resolution of NPPW$_x = 21$ and NPPW$_y = 32$ was used for this simulation. Similarly to the 0.5 kHz calculation of the previous case, the calculations became invariably unstable when the solutions for the other frequencies were sought. The numerical instabilities were more violent at this Mach number because of the stronger discontinuities in the normal velocities in the LE and TE regions of the liner. The effects of a discontinuity on the solutions are amplified by the term $u_0 \partial v/\partial x$ in the normal momentum and impedance condition equations. Figure 16 illustrates the growth of the normal velocity discontinuity at the liner LE at the $M = 0.5$ and $f = 0.5$ kHz conditions.

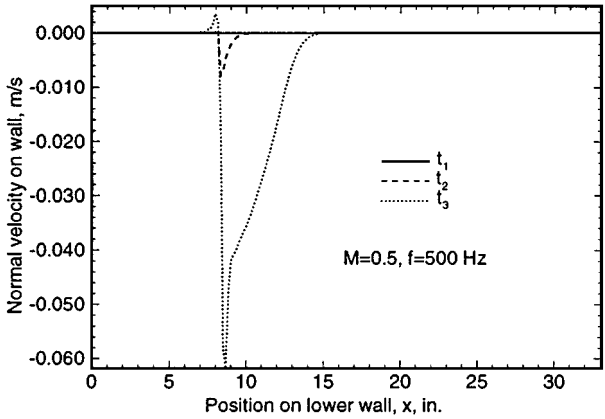

FIG. 16. Discontinuous normal velocity, shown at increasing times, due to hard-soft wall transition. $M = 0.5$, $f = 0.5$ kHz.

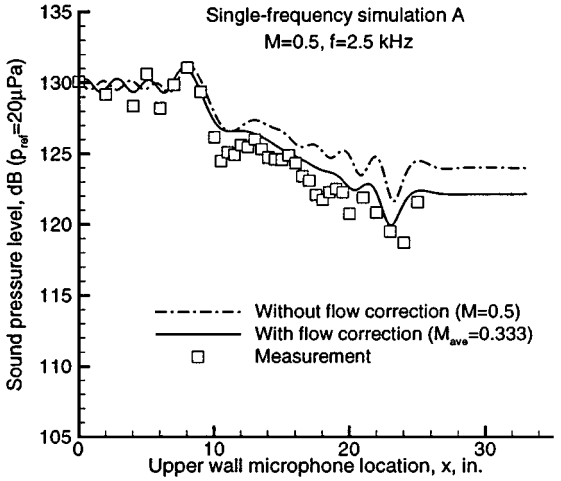

FIG. 17. Upper wall SPL at 2.5 kHz and $M = 0.5$ with and without mean-flow correction. CFL $= 0.5$, $\text{NPPW}_x = 21$. Second-order scheme with $\beta = 0$, $\sigma = 0$ used.

It is, however, interesting that the computations remained stable at 2.5 kHz. This is perhaps because the liner response changes with the wave frequency and the 2.5 kHz frequency did not give rise to as strong discontinuities as the other frequencies. The results are shown in Fig. 17, together with the measurement. The discrepancy between the calculation and the data appears to have increased considerably at this Mach number. As was explained above, the main reason for this discrepancy is the usage of the peak mean-flow velocity from the measurement. The mass deficits due to the boundary layers of these fully developed channel flows were not taken into account. We can partially correct for this using an average velocity. A parabolic velocity profile assumption yields an average speed of $M_{\text{ave}} = \frac{2}{3}M$. The result of the calculations using this average value for the $M = 0.5$ case is also shown in Fig 17. It is evident that a significant improvement has been gained in the prediction compared to experiment. The agreement between the simulation and the data is now reasonably good. Therefore, using the average velocity values for the $M = 0.1$ and $M = 0.3$ cases should also improve their predictions.

4.3. Computational Cost

The present method was initially programmed using CM Fortran and run on the Thinking Machines CM-200 and CM-5 computers. Since these computers are no longer available and also for portability reasons, the code has been converted to Fortran 90. It can now be run on many computing platforms. For example, a typical simulation on a 188×14 mesh (with 86 grid points on the soft wall) using 20,000 time steps required about 0.67 h of CPU time on an SGI Power Challenge R10000 processor. The share of the wall boundary conditions (both hard and soft) in this cost was only 2.6%, i.e. 0.017 h, of which only 26% was spent on the calculation of $R^{n,n-1,\cdots}$ given by Eq. (26). This simulation used the broadband-frequency function $Z_B(z)$, which has $M_N = 5$ and $M_D = 4$ as shown in the Appendix. It is clear that the doubling of these parameters would require only very minor additional CPU time and still efficient computations would be achieved. For this example calculation, the fourth-order spatial discretization and the bilinear approximation for the time-derivative term of the impedance condition were employed. Therefore, a penta-

diagonal equation system was needed to be inverted at every R-K stage. It is clear that the spatially second-order scheme would require considerably less CPU time. It should be noted that a single-frequency simulation is as costly as a broadband calculation.

5. CONCLUDING REMARKS

The ability to apply impedance conditions in time-domain numerical methods is extremely important for applications with acoustic treatment. For this purpose, an efficient time-domain method has been developed using the z-transform. Specifically, the standard frequency-domain impedance condition has been converted to the time domain as only IIR type, digital filter operations. This has been accomplished by modeling the impedance by a rational function in the z-domain. The resultant impedance condition uses only limited past acoustic pressure and normal velocity knowledge as well as the current normal velocity. The incorporation of this time-discretized impedance condition into the four-stage Runge–Kutta time-integration scheme has been discussed.

Three different time-derivative operators have been used in the z-domain to formulate the discrete-time domain impedance condition. These are the first-order backward, second-order central difference, and the bilinear operators. Although these are low order approximations, the impedance condition has been incorporated into the fourth-order R-K scheme. The use of the fourth-order R-K scheme in concert with the lower order discretizations of the boundary conditions leads to better accuracy than the use of a lower order time-integration scheme would. The use of the backward difference or bilinear operator results in an implicit time-discretized impedance condition when flow exists. Although this is not the case with the second-order operator, its use has been found to generate unstable solutions in the presence of flow. The bilinear approximation is more accurate than the first-order backward difference in general. However, numerical tests using various CFL numbers indicated both of these approximations yield equally acceptable solutions.

The developed method has been validated by numerical simulations of the NASA Langley flow-impedance tube at various frequencies (from 0.5 to 3.0 kHz) and flow conditions (from $M = 0.0$ to 0.5). The present work represents the first attempt to solve such a problem in the time domain. The simulations used a uniform background flow assumption with the mean-flow centerline velocities. The results indicated excellent agreement at relatively low Mach numbers with this assumption. However, because of this assumption, some discrepancies were observed between the simulated results and experiment as the Mach number was increased. It has been shown that the use of corrected or averaged velocities improve the results at higher Mach numbers significantly.

Also, it was found that the simulation of the flow-impedance tube could be hindered at some flow conditions by numerical instabilities that are triggered by the infinitely large impedance jumps in the transitional regions of the soft and hard walls. Although these instabilities could partially be suppressed in one case by only decreasing the mesh resolution, the results still presented shock-like spurious waves at the LE and especially TE of the liner, causing poor prediction of the upper wall SPL. These instabilities could be removed by smooth transitions in both the resistance and reactance. It is, therefore, desirable to have the capability to treat full spatial variation in impedance.

Finally, the standard formulation of the impedance condition (particle displacement continuity) has been shown to accurately describe the linear physical phenomena over acoustically treated surfaces both with and without flow.

APPENDIX

Impedance of the constant depth ceramic tubular liner (CT73). The impedance of the liner used in the NASA Langley flow-impedance tube simulations is given in Table 1 below. The curves shown in Fig. 1 in Section 2.2 were obtained applying a nonlinear least square fit to the frequency-domain impedance function given by Eq. (15). The parameters r_1 to r_7 of this equation were found to be

$$\begin{aligned} r_1 &= 0.34688814087644 \\ r_2 &= 109.94771953585 \\ r_3 &= 1.662 \times 10^{-2} \\ r_4 &= 8.9946186703464 \times 10^{-5} \\ r_5 &= 1.8996348959126 \times 10^{-5} \\ r_6 &= 12379.898172461 \\ r_7 &= 6.6949280013217 \times 10^{-5}. \end{aligned} \tag{36}$$

Broadband-frequency impedance function. The z-domain impedance function $Z(z)$ is obtained by the substitution of $(1-z^{-1})/\Delta t$ into the frequency-domain impedance function (Eq. (15)) for the $i\omega$ term. Since the z-domain approximation of the $i\omega$ term contains a Δt term, the resultant function $Z(z)$ will be Δt dependent. Therefore, the time step size of each particular run will affect the constant parameters of $Z(z)$. The time step size for most of the broadband-frequency runs was taken to be $\Delta t = 1/(512\,f)$, where $f = 500$ Hz. Thus, the impedance function $Z_B(z)$ of Section 3 for this time step size was

$$\frac{Z_B(z)}{\rho_0 c_0} = \frac{\bar{a}_0 + \bar{a}_1 z^{-1} + \bar{a}_2 z^{-2} + \bar{a}_3 z^{-3} + \bar{a}_4 z^{-4}}{1 - b_1 z^{-1} - b_2 z^{-2} - b_3 z^{-3}}, \tag{37}$$

where

$$\begin{aligned} \bar{a}_0 &= 17.5647781535215 \\ \bar{a}_1 &= -69.4730957492080 \\ \bar{a}_2 &= 103.156370589274 \\ \bar{a}_3 &= -68.1512164562849 \\ \bar{a}_4 &= 16.9032230636361 \\ b_1 &= 2.98393221010723 \\ b_2 &= -2.97017509982092 \\ b_3 &= 0.986242347629329. \end{aligned} \tag{38}$$

TABLE 1
Measured and Fitted Specific Resistance and Reactance Values for the Constant Depth Ceramic Tubular Liner (CT73)

Frequency kHz	$R/\rho_0 c_0$ (exp.)	$R(\omega)/\rho_0 c_0$ (fit)	$X/\rho_0 c_0$ (exp)	$X(\omega)/\rho_0 c_0$ (fit)
0.5	0.41	0.406	−1.56	−1.587
1.0	0.46	0.476	0.03	0.113
1.5	1.08	1.078	1.38	1.638
2.0	4.99	5.009	0.25	−0.276
2.5	1.26	1.263	−1.53	−1.237
3.0	0.69	0.673	−0.24	−0.286

Single-frequency impedance function. The substitution of $(1 - z^{-1})/\Delta t$ into Eq. (34) $(Z(\omega)/\rho_0 c_0 = R_0 + i\omega\, a + b/i\omega)$ for $i\omega$ results in

$$\frac{Z_S(z)}{\rho_0 c_0} = \frac{\bar{a}_0 + \bar{a}_1 z^{-1} + \bar{a}_2 z^{-2}}{1 - z^{-1}}, \tag{39}$$

where

$$\begin{aligned} \bar{a}_0 &= R_0 + a/\Delta t + b\Delta t \\ \bar{a}_1 &= -(R_0 + 2a/\Delta t) \\ \bar{a}_2 &= a/\Delta t. \end{aligned} \tag{40}$$

ACKNOWLEDGMENTS

This work was supported by the NASA Langley Research Center Grant NAG-1-1367. The computational resources (CM-5) were provided by the National Center for Supercomputing Applications at the University of Illinois at Urbana-Champaign. Also, the authors would like to thank P. J. Morris of the Pennsylvania State University for useful discussions.

REFERENCES

1. Y. Özyörük, *Sound Radiation from Ducted Fans Using Computational Aeroacoustics on Parallel Computers*, Ph.D. thesis, Pennsylvania State University, December 1995.
2. Y. Özyörük and L. N. Long, A new efficient algorithm for computational aeroacoustics on parallel processors, *J. Comput. Phys.* **125**(1), 135 (1996).
3. Y. Özyörük and L. N. Long, Computation of sound radiating from engine inlets, *AIAA J.* **34**(5), 894 (1996).
4. Y. Özyörük and L. N. Long, Multigrid acceleration of a high-resolution computational aeroacoustics scheme, *AIAA J.* **35**(3), 428 (1997).
5. R. E. Motsinger and R. E. Kraft, Design and performance of duct acoustic treatment, in *Aeroacoustics of Flight Vehicles: Theory and Practice*, NASA Ref. Pub. 1258, Vol. 2, (NASA, Washington, DC, 1991).
6. T. L. Parrott and M. G. Jones, Parallel-element liner impedances for improved adsorption of broadband sound in ducts, *Noise Control Engineering J.* **43**(6), 183 (1995).
7. T. L. Parrott, W. R. Watson, and M. G. Jones, *Experimental Validation of a Two-Dimensional Shear-Flow Model for Determining Acoustic Impedance*, Technical report TP-2679 (NASA, Washington, DC, 1987).
8. T. L. Parrott, A. L. Abrahamson, and M. G. Jones, *Measured and Calculated Acoustic Attenuation Rates of Tuned Resonator Arrays for Two Surface Impedance Distribution Models with Flow*, Technical report TP-2766 (NASA, Washington, DC, 1988).
9. W. R. Watson, M. G. Jones, S. E. Tanner, and T. L. Parrott, Validation of a numerical method for extracting liner impedance, *AIAA J.* **34**(3), 548 (1996).
10. W. R. Watson, M. G. Jones, S. E. Tanner, and T. L. Parrott, A finite element propagation model for extracting normal incidence impedance in nonprogressive acoustic wave fields, *J. Comput. Phys.* **125**, 177 (1996).
11. Y. Özyörük and L. N. Long, A time-domain implementation of surface acoustic impedance condition with and without flow, *J. Comput. Acoustics* **5**(3), 277 (1997).
12. C. K. W. Tam and L. Auriault, Time-domain impedance conditions for computational aeroacoustics, *AIAA J.* **34**(5), 917 (1996).
13. D. M. Sullivan, Frequency-dependent FDTD methods using Z transform, *IEEE Transactions on Antennas and Propagation* **40**(10), 1223 (1992).
14. C. Penney, *Scattering from Coated Targets Using a Frequency-Dependent Impedance Boundary Condition in the Finite-Difference Time-Domain Method*, Ph.D. thesis, Pennsylvania State University, University Park, PA, May 1995.

15. M. K. Myers, On the acoustic boundary condition in the presence of flow, *Journal of Sound and Vibration* **71**(3), 429 (1980).
16. A. V. Oppenheim and R. W. Schafer, *Discrete-Time Signal Processing* (Prentice-Hall, Englewood Cliffs, NJ, 1989).
17. B. J. Tester, The propagation and attenuation of sound in lined ducts containing uniform or "plug" flow, *Journal of Sound and Vibration* **28**(2), 151 (1973).
18. M. B. Giles, Nonreflecting boundary conditions for Euler equation calculations, *AIAA J.* **28**(12), 2050 (1990).
19. A. D. Pierce, *Acoustics —An Introduction to Its Physical Principles and Applications* (Acoustical Society of America, New York, 1989).
20. W. H. Press, S. A. Teukolsky, W. T. Vetterling, and B. P. Flannery, *Numerical Recipes in Fortran* (Cambridge University Press, New York, second edition, 1992).
21. C.-J. Hwang and D.-J. Lee, Transparent acoustic source condition applied to the Euler equations, *AIAA J.* **33**(9), 1736 (1995).